



Research Article

Effect of induced defects on the properties of ZnO nanocrystals: surfactant role and spectroscopic analysis

Debika Devi Thongam¹  · Jagriti Gupta²  · Niroj Kumar Sahu¹ 

© Springer Nature Switzerland AG 2019

Abstract

Semiconductor photocatalysts are one of the major sought area of research due to their extensive use in the degradation of organic pollutants under UV–visible and solar light. Herein, we are reporting the synthesis of microscopic spindle shaped ZnO photocatalysts with different reducing agents such as sodium hydroxide, hydrazine hydride, sodium borohydride and lithium triethyl borohydride. These spindle shaped ZnO are synthesized by facile soft chemical approach by varying reducing agents with fixed molar ratio at 1:2 zinc precursor to reducing agents. These ZnOs were thoroughly characterised by various sophisticated characterization techniques such as XRD, FTIR, SEM, and HRTEM, Raman and ESR spectroscopies. Microscopic results show that these ZnO show similar fusiform morphologies with the variation in sizes and their distributions, and hence possess different defect related properties. The structural growth mechanism and defect related properties were explained on the basis of different reducing abilities of reducing agents (different reaction pH) and their nucleation with the aid of morphological analysis, and ESR analysis. Furthermore, the photocatalytic activity of these spindle shaped ZnO were evaluated against two cationic dyes (methylene blue dyes, Rhodamine B) under UV light. The photocatalytic results show that these spindle shaped ZnO are very effective for the photo-catalytic degradation of methylene blue and rhodamine B dye under the illumination of UV light.

Keywords ZnO · Reducing agents · Defects · Annealing · Photocatalytic degradation · Methylene blue · Rhodamine B

1 Introduction

Nowadays, wide bandgap transition metal oxide semiconductor nanomaterials like ZnO, SnO₂, TiO₂, CuO, WO₃ etc. are increasingly gaining the limelight of today's research field as they have unique surface, optical, electrical, magnetic and others properties [1–7] that are limited to their nano regime but found to be almost insignificant in their bulk counterparts. Because of their exceptional properties in comparison to their difference [6] in bulk analogue, semiconductor photocatalyst materials are potentially

used in various applications like solar cells [8], electrode materials [9, 10], sensors [11, 12], optical imagings [13], UV absorbers [14], photo-catalysis [15–19] etc. [2]. The photocatalyst materials can be employed either in their pristine form or after doping with a third element such as silver, copper, gold, iron, nitrogen or in the form of hybrid photocatalyst like core–shell structures to enhance the efficiency [6, 17–24]. However, even there are additional benefits provided by doping of metals to semiconductor oxides and making hybrid photocatalyst materials, these processes need cumbersome preparation steps, and hence it

Debika Devi Thongam and Jagriti Gupta have contributed equally to this work.

Electronic supplementary material The online version of this article (<https://doi.org/10.1007/s42452-019-1058-3>) contains supplementary material, which is available to authorized users.

✉ Niroj Kumar Sahu, nirojs@vit.ac.in | ¹Centre for Nanotechnology Research, Vellore Institute of Technology, Vellore 632014, India. ²Chemistry Division, Bhabha Atomic Research Centre Bombay, Mumbai 400085, India.



SN Applied Sciences (2019) 1:1030 | <https://doi.org/10.1007/s42452-019-1058-3>

Received: 20 May 2019 / Accepted: 7 August 2019 / Published online: 14 August 2019

is mostly desirable to engineer and manipulate the desired properties in a minimal approach. Thence, a simple facile chemical synthesis technique is used to synthesize multiple pristine ZnO nanoparticles with a comparable photocatalytic efficiency without doping and incorporating with other materials and in the absence of separate surfactants.

ZnO is a II–IV n-type direct wide band gap semiconductor compound with 3.37 eV and ~60 meV exciton binding energy [25]. ZnO, one of the most remarkable material displays exclusive material properties in magnetic, optical, surface etc. with the change in morphologies, presence of crystal/native defects, crystallite/particle sizes and various other factors as its material properties tenability is found to be achieved in different ways [26–30]. Therefore, there is a profound need to investigate and understand the change of structural, chemical and physical properties of ZnO semiconductor material. From the past decades, many researchers used innumerable techniques to study magnetic and optical properties but the origin of these properties in pristine ZnO structure still remains controversial. Even though most of the researchers pointed the origin of these magnetic and optical properties are due to the presence of defects [30], further investigation is still required to understand and investigate different type of defects (oxygen and zinc vacancies, zinc interstitials etc.) that caused to show these remarkable behaviours. These in-depth study of material properties assist in understanding the catalytic effect towards dye degradation like methylene blue [3, 31] and rhodamine B [32, 33]. As chemical or synthetic dyes are preferred over natural dyes industrially due to the formation of stable bonding between fabric and dye molecules retaining for a long period of time, it becomes a crucial environmental concern. The waste dyes from textile industries when mixed with water sources like oceans, rivers, lakes, underground water etc., creates toxic substances causing different diseases when consumed directly or indirectly. Most of the commonly used basic chemical dyes to study photo-catalytic degradation are methylene blue and rhodamine B which are taken as model dyes here to study because of its high toxicity, accumulation and retaining capability to the added environment.

Herein, we are reporting the preparation of highly crystalline and pristine zinc oxide by a simple facile chemical approach using different reducing agents in ethylene glycol medium which work as structural directing and a surfactant to inhibit the aggregation. This work is the continuation of the previously published work [15] with the in-depth property studies of pristine zinc oxides and their photocatalytic behaviour towards other dye i.e. Rhodamine B (RhB) [13]. The microstructurals, chemical, defects and optical properties of these ZnO samples are explored using different characterisation techniques specifically

XRD, SEM, TEM, HRTEM, FTIR, Raman, and ESR spectroscopy. These zinc oxides are annealed at 300 °C before studying the photo-catalytic degradation and decolourisation of both cationic dyes; methylene blue and rhodamine B in presence of UV light are studied. This photocatalytic dye degradation is based on the batch system reactions. As the variation in dye molecular structure can alter the degradation process by declining or increasing in degradation rate, it is very crucial to study the interaction of different dye molecules and a certain photocatalyst material to inspect the catalyst validity to other dyes without introducing external acidic or basic agents. Due to the lack of comparison study of different dyes degradation using pristine single transition element semiconductor photocatalyst based on the performance and dye-catalyst interaction, it is very crucial to explore and investigate [34–37]. Herein, a comparative study in the dissimilarity of degradation time consumption by non-identical dyes are exhibited elaborately in the discussion section based on the properties of dyes and its interaction with catalyst material during the photocatalytic dye degradation process. The effect of annealing the photocatalyst before utilizing in degradation reaction is also discussed and compared accordingly based on the degradation rates.

2 Experimental section

2.1 Materials synthesis

ZnO nanoparticles were synthesized from zinc acetate; $\text{Zn}(\text{CH}_3\text{COO})_2$ zinc precursor and NaOH or N_2H_4 or NaBH_4 or $\text{Li}(\text{C}_2\text{H}_5)_3\text{BH}$ as reducing agents in the molar ratio of 1:2 in ethylene glycol medium as reported in the previous publication [15]. All the reagents and chemicals used in this process are analytically graded and no further purifications are carried out. $\text{Zn}(\text{CH}_3\text{COO})_2$, N_2H_4 , $\text{Li}(\text{C}_2\text{H}_5)_3\text{BH}$ are obtained from Sigma-Aldrich. Ethylene glycol, NaOH, and NaBH_4 are bought from Merck Pvt. Ltd., India. Throughout the process Milli-Q water was used.

In 500 ml three neck conical flask, 100 ml of ethylene glycol was taken and 5 mM of $\text{Zn}(\text{CH}_3\text{COO})_2$ was added to it under continuous magnetic stirring in oil bath and heated to 60–70 °C for 30 min. A 10 mM NaOH solution was prepared in 5 ml ethylene glycol with the help of sonication. NaOH solution was added to zinc precursor reaction solution in drop wise. After addition of reducing agent solution, transparent $\text{Zn}(\text{CH}_3\text{COO})_2$ solution is transformed into a milky white colour solution indicating the formation of zinc hydroxides. Crystalline ZnO nanoparticles were able cultivate when refluxed at 150 °C for 2 h. The samples were washed repeated times with milli-Q water and nanoparticles were collected through centrifugation. The washed

aggregated ZnO samples were dried for 8 h at 100 °C before continuing further characterizations. The ZnO samples prepared using NaOH, N₂H₄, NaBH₄ and Li(C₂H₅)₃BH were referred in the text as ZnO–NaOH, ZnO–N₂H₄, ZnO–NaBH₄, and ZnO–Li(C₂H₅)₃BH, respectively.

2.2 Materials characterization

The purity, crystallinity, crystallite size and lattice microstrain of these pristine ZnO samples are analyzed by powder X-ray Diffraction technique recorded in PhilipsPW3040/60. The crystallite sizes and lattice strain were approximated by adopting Debye–Scherrer's equation with full width half maxima value and Williamson and Hall equation. The chemical properties like the presence of functional groups are shown by taking Fourier transform infrared spectroscopy (FTIR, Magna 550, Nicolet Instruments Corp). Physical properties like morphology and surface structure of ZnO samples are observed using scanning electron microscopy (SEM, JSM-7600F FEG SEM). The crystal lattice structural properties like defects, compositions etc. were determined from Raman spectroscopy measured by using Lab RAM HR 800 for 200–800 cm⁻¹ Raman shift range. To analyse the presence of unpaired electrons and defects, the samples were analysed and discussed by electron spin resonance (ESR) spectroscopy (JES-FA200 ESR Spectrometer). A Philips TUV 25W/G25T8UV tube light of wavelength 365 nm is used for photo-catalytic dye degradation of methylene blue and rhodamine B dyes by illuminating directly to the dye solution.

2.3 Dye degradation

Photo-catalytic degradation of both the cationic organic dyes rhodamine B (RhB) and phenothiazine derivative methylene blue (MB) are carried out under the influence of UV light illumination in a dark close box as a batch system reaction. Here, 100 ml of 10 ppm (parts per million) MB solution is taken in a flat bottom glass flask. 50 mg of the synthesized and annealed ZnO–NaOH is added to the dye solution and is kept for 15 min sonication to make ZnO–NaOH equally dispersed in dye solution in a controlled manner (no light is allowed to enter inside the reaction chamber). The dye and photocatalyst solution mixture is kept above a magnetic stirrer under the UV lamp and started stirring continuously for 15 min before UV illumination. During photo-catalytic reaction with the illumination of UV light, 1 ml of dye solution is taken out is an aliquot in every 10 min interval time until complete decolouration takes place. The collected aliquots are centrifuged for 10 min to filter catalysts material from dye solution. The supernatant is taken out to study catalytic degradation of dyes in presence of catalyst using UV–visible absorption

spectra with reference to milli-Q water. The absorption spectra of each samples are compared accordingly with respect to the time taken for complete dye decolouration for all samples. The same process is carried out for the other three remaining annealed zinc oxide samples and RhB. The whole dye degradation reaction process took place at room temperature.

3 Results and discussion

Figure 1a shows the comparison of XRD patterns of the synthesized ZnO samples. XRD spectra reveals three sharp prominent peaks which corresponds to (101), (100) and (002) planes. These distinct peaks confirm complete formation of wurtzite phase structure of ZnO without any impurities as per the JCPDS reference code: 00-036-1451 with the lattice constant value of $a = 3.2498 \text{ \AA}$, $b = 3.2498 \text{ \AA}$ and $c = 5.2066 \text{ \AA}$. The resulted ZnO nanoparticles show highly crystalline nature with average crystallite sizes of 24, 23, 26 and 22 nm for ZnO–NaOH, ZnO–N₂H₄, ZnO–NaBH₄, and ZnO–Li(C₂H₅)₃BH respectively, calculated from Scherrer's formula (given by Eq. 1) using full width half maxima (FWHM) values. The Debye–Scherrer's formula is given by:

$$d = \frac{\lambda\kappa}{b\cos\theta} \quad (1)$$

where d crystallite size in nm, λ wavelength of Cu-K α radiation = 0.15416 nm, b = full width half maxima in radian, κ = constant = 0.9, θ = angle of scattering in degree.

The inset of Fig. 1 shows the enlarged image of the three prominent XRD peaks (100), (002), and (101) of ZnO samples. The enlarged inset figure showed significant differences in full width half maxima (FWHM) and intensities of three prominent peaks of all samples. The intensity of these peaks of different ZnO samples prepared are found to be different. The ZnO structure resulted from using borohydride derivatives namely ZnO–NaBH₄ and ZnO–Li(C₂H₅)₃BH have larger FWHM and stronger intensity as compared to zinc oxides prepared with N₂H₄ and NaOH therefore resulted in smaller crystallite size as average crystallite size is inversely proportional to FWHM value and Bragg angle in Debye–Scherrer's formula. The intensity ratios of the prominent peaks (I_{101}/I_{002}) are 2.5, 1.8, 1.7, and 1.5 for ZnO–NaOH, ZnO–N₂H₄, ZnO–NaBH₄, and ZnO–Li(C₂H₅)₃BH, respectively. From the calculated value of I_{101}/I_{002} , ZnO samples prepared with borohydride derivative i.e. Li(C₂H₅)₃BH have the lowest value, and largest with the presence of NaOH in which this same effect can be seen in average crystallite size. This analogous behaviour of this intensity ratio and crystallite size relation can be credited by the effect of different reducing agents as well as the basicity of reaction medium during Zn(OH)₂

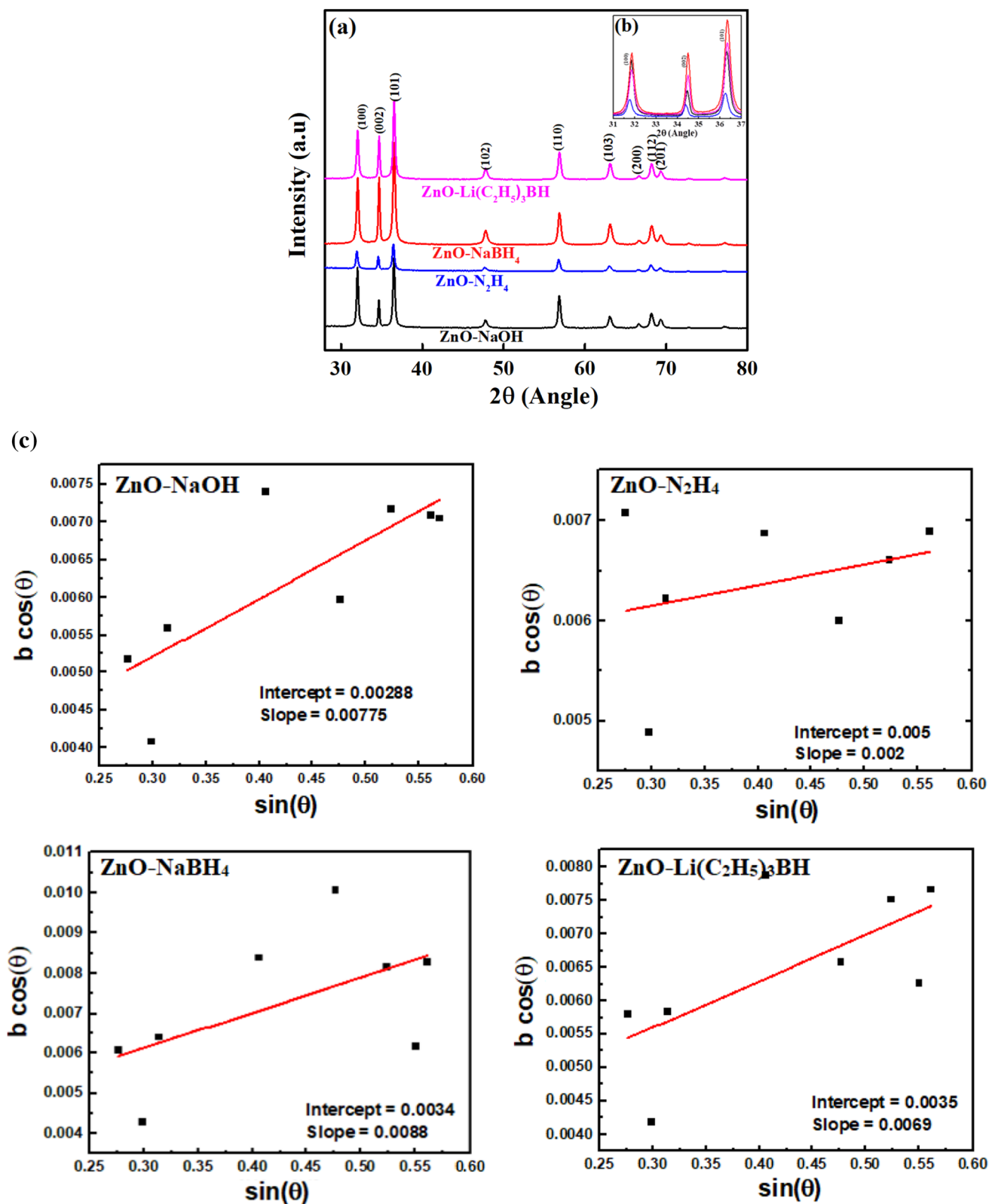


Fig. 1 **a** XRD patterns of ZnO samples, **b** enlarged portion of three prominent peaks and **c** W-H plot showing intercept and slope value

formation. And it can also be affected by the presence of –OH group in NaOH and highly basic nature of N_2H_4 which helped in (101) directional crystal growth and growth inhibition respectively. The crystallite size and lattice micro-strain were also calculated from a classical method called Williamson and Hall (W–H) method, an integral breadth method where peak width is taken as a function of 2θ (2θ). As the crystals are of finite sizes, they are commonly known to be imperfect crystals as perfect crystals are found to be extended infinitely in all directions. Therefore, the broadening in XRD diffraction peaks are due to the sum (given by the Eq. 4) of instrumental and nanocrystal material dependent effects (given by the Eq. 3) originated from the crystal imperfections and can be corrected by following Eq. 5. The crystallite size-lattice strain related graph or W–H graph given by the Eq. 6 is plotted in terms of $b\cos(\theta)$ on x-axis against $\sin(\theta)$ on y-axis from the data collected corresponding to the prominent peaks of ZnO XRD patterns. By Williamson and Hall, the broadening in XRD can be corrected by

$$b = \sqrt{b_{measured}^2 - b_{instrumental}^2} \quad (2)$$

where b corrected instrumental broadening.

The strain induced broadening is given by the following formula (Eq. 3):

$$\varepsilon = \frac{b}{4\tan\theta} \quad (3)$$

$$b = \text{crystallite size contribution} + \text{lattice strain contribution} \quad (4)$$

$$b = \frac{\lambda\kappa}{d \cos \theta} + 4\varepsilon \tan \theta \quad (5)$$

$$b \cos \theta = \frac{\lambda\kappa}{d} + 4\varepsilon \sin \theta \quad (6)$$

The W–H analysis plot displays Lorentzian profiles following Uniform Deformation model (UDM), considering the crystal shows isotropic nature where uniform strain is distributed in all the crystallographic directions. From the W–H analysis linear fitting graph, the intercept in y-axis

and the slope of straight line gives crystallite size and lattice micro-strain values (given by Eq. 6). Table 1 gives the crystallite sizes calculated for all the ZnO samples by using Scherrer's formula and W–H plot, and their lattice strain values. As Debye-Scherrer's formula gives the lower bound of crystallite sizes and although XRD peak positions are similar (due to same chemical compositions and physical properties), a significant difference in intensities and peak broadness are seen. The small shift and broadening in peaks seen in Fig. 1 are due to the presence of lattice micro-strain effect and crystallographic size origin broadenings which may be attributed to the strain produced by the uses of different reducing agents in the $Zn(OH)_2$ nucleation and growth reaction stages. The deviation in these crystallite sizes calculated from two different approaches are due to the introduction of lattice strain in Williamson and Hall method and the varying value is found to be small in magnitude which is contributed to the averaging difference in particle sizes distribution. From Fig. 1c, it is evident that Williamson and Hall approach gives a positive slope i.e. positive strain and a finite intercept value (non-zero) [38–42].

A non-destructive FTIR spectroscopy technique is used to study the vibrational behaviour of bonding in organic molecules as well as in metal–oxygen bond in metal oxides. This technique is used to identify the presence of impurities, specific functional groups and bonding originated from the chemisorption of organic molecules on nanoparticle surfaces that took place during nanoparticle synthesis process and during spectroscopy study. Here, Fig. 2 shows the FTIR spectra of ZnO samples. The band located between 421 and 559 cm^{-1} corresponds to Zn–O stretching mode which confirms the formation of ZnO. From the FTIR spectra, the presence of –OH bending and stretching vibration peaks are evident at 890 cm^{-1} and 3349 cm^{-1} , as IR absorbance by –OH stretching is found to be strong and broad as compared to bending inevitably [43–46]. These –OH bending and stretching vibration peaks are originated from H_2O and glycol functionalization in ZnO crystal surfaces which acts as a surfactant in ZnO preparation and moisture content in the air [15]. Though the FTIR pattern of all samples show similar peak positions without any shift, the broadness and intensity of –OH

Table 1 Crystallite sizes, lattice strain and intensity ratio of the synthesized samples

Sl. No.	Sample name	d in nm (Debye–Scherrerr's formula)	d in nm (Williamson and Hall formula)	Lattice strain (Williamson and Hall formula)	I_{101}/I_{002}
1.	ZnO–NaOH	24	28	0.00775	2.5
2.	ZnO– N_2H_4	23	50	0.00204	1.8
3.	ZnO– $NaBH_4$	26	34	0.00884	1.7
4.	ZnO– $Li(C_2H_5)_3BH$	22	35	0.00695	1.5

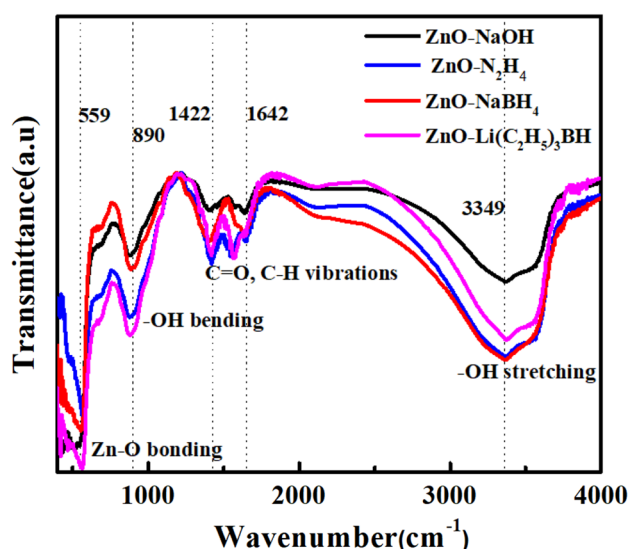


Fig. 2 FTIR spectra of different ZnO nanoparticles

stretching corresponding to 3349 cm^{-1} differs for different samples prepared with different reducing agents. Hence, it can be inferred that the variation in peak broadness and intensities are found to be due to the presence of unequal quantity of specific -OH functional groups chemisorbed in

ZnO surfaces as the basicity of the reaction medium is varied by varying the type of reducing agents. ZnO prepared with NaOH shows less broadness and minimum intensity while that prepared with NaBH_4 and N_2H_4 show stronger corresponding peak which show the effect of basicity reaction medium caused by the addition of reducing agents. This basicity of the reaction medium influenced the quantity of -OH functional groups attaching in Zn(OH)_2 nuclei during growth process. The peaks present at 1422 cm^{-1} and 1642 cm^{-1} show C=O and C-H vibration bands due to the presence of partially transformed aldehyde or ketone groups are contributed from the zinc source acetate ions ($\text{Zn(CH}_3\text{COO)}_2$) as well as the glycol functional group coatings [3, 47].

The morphologies of ZnOs are analysed using FESEM images. The prepared samples with N_2H_4 , NaBH_4 , and $\text{Li(C}_2\text{H}_5)_3\text{BH}$ reducing agents show complete formation of spindle shape morphology which resembles like a fusiform muscle (Fig. 3b–d). However, the central belly thickness of ZnO prepared with NaOH is seen to be ununiformly distributed. The ZnO–NaOH fusiform structure’s central belly is seen to be located near one end of tendon inappropriately as compared to the original fusiform structure (Fig. 3a inset figure). The tendons are also seen to be blunt comparing with the ones resulted

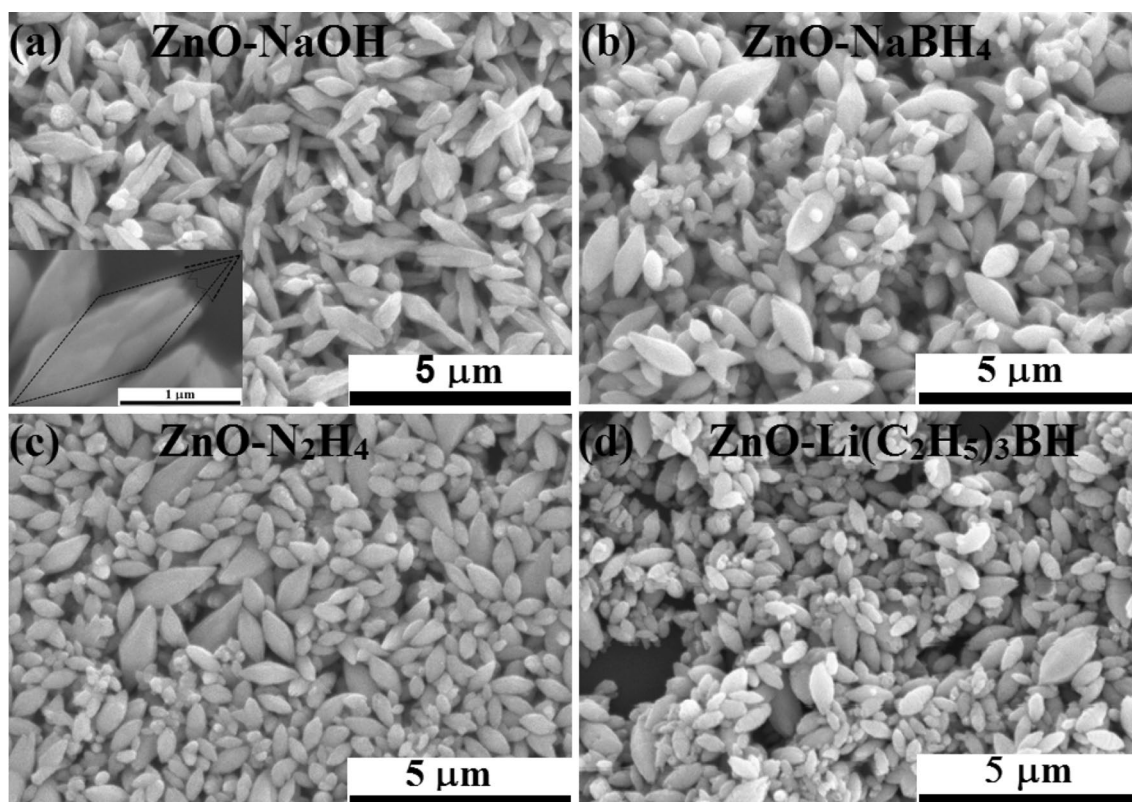


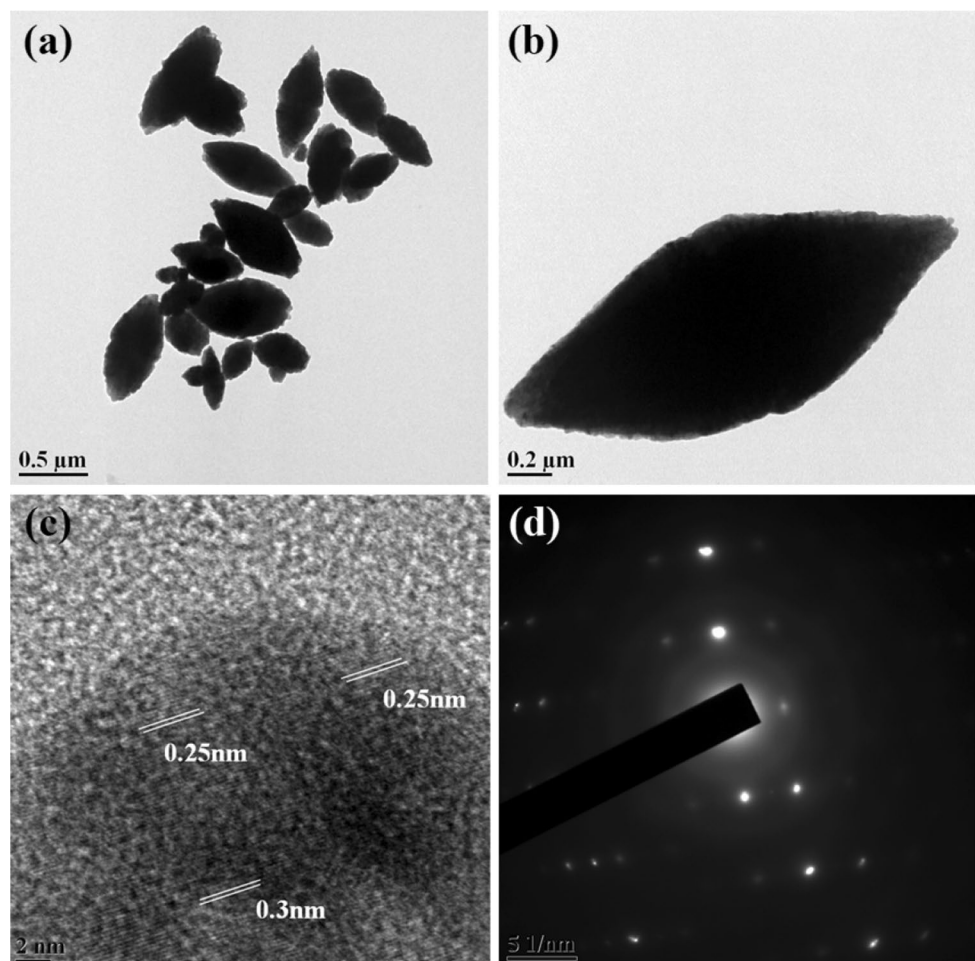
Fig. 3 SEM images of **a** ZnO–NaOH (inset **a** fusiform structure of ZnO), **b** ZnO– NaBH_4 , **c** ZnO– N_2H_4 , and **d** ZnO– $\text{Li(C}_2\text{H}_5)_3\text{BH}$

from using other three reducing agents. The variation in size distribution of ZnO spindles as well as shape is due to the variation in nucleation and growth rate of $\text{Zn}(\text{OH})_2$ in different pH of the reaction solution. This nucleation and growth mechanism has been thoroughly described in the previous published paper work [15]. The dimensions of ZnO–NaOH spindles are; 2–3 μm in length and $\sim 0.5 \mu\text{m}$ in central belly width (Fig. 3a). It has been clearly visible from the FESEM images that the outer surface of ZnO–NaOH fusiform is found to be irregular with more crests and troughs or ridges. In some structures, tendon end shows incomplete growth. ZnOs prepared with N_2H_4 , NaBH_4 , and $\text{Li}(\text{C}_2\text{H}_5)_3\text{BH}$ show the formation of variable size fusiforms, where ZnO– $\text{Li}(\text{C}_2\text{H}_5)_3\text{BH}$ show the smallest size morphologies with 0.5–1.5 μm in length and 90% equal size distribution with blunt tendons. From Fig. 3, it is evident that ZnO particles do not form aggregates. This behaviour may be contributed to the surfactant property of glycol molecules present in ZnO reaction medium decorating the ZnO nanoparticles (shown and discussed in depth in previous publication with an illustrated mechanism) [15]. To further study the crystal structures

and morphologies, TEM, HRTEM and SAED pattern have been analysed (for ZnO– N_2H_4 sample). Figure 4 shows the TEM and HRTEM images of ZnO fusiform structures. The d-spacing of around 0.25 nm is matching with the (002) plane having an interlayer spacing of 0.25 nm planes of ZnO (Fig. 4c). The HRTEM image also shows sign of high crystallinity with no crystal dislocations. The crystallinity of ZnOs were confirmed by the SAED pattern that exhibit a ring pattern (Fig. 4d) and also variable size distribution and surface roughness have been identified from Fig. 4a.

Raman spectroscopy is an excellent technique in which elementary excitations (vibrational, rotational, and other low-frequency modes) are detected by scattering of phonons at room temperature. It also conveys information on structural properties, chemical compositions, orientations, and crystalline qualities. The basic unit of wurtzite-type ZnO lattice structure has 4 atoms per primitive cell (n) ($n=2$ in zinc blende lattice structure) and it is found that the dispersion relation along hexagonal axis was procured by folding corresponding zinc blende crystal along (111) direction. As $n=4$ atoms per unit cell in wurtzite structure, the number of phonons branches are equal to 12 ($3n$); 3

Fig. 4 TEM and HRTEM image of ZnO fusiform structure; **a** ZnOs with variable sizes, **b** completely formed individual ZnO fusiform structure and **c, d** higher resolution image and its SAED pattern of ZnO



acoustic modes (one longitudinal acoustic, two transverse acoustic modes) and $3n - 3 = 9$ optical phonons (three longitudinal optical, six transverse optical modes). The following group theory shows the optical phonons expression [48] at Γ -point of Brillouin zone:

$$\Gamma_{opt} = A_1 + 2B_1 + E_1 + 2E_2 \tag{7}$$

This group theory given by Eq. 7 shows that near Γ -point of Brillouin zone, there are four branches; a single A_1 branch, single-doubly and two-doubly degenerate E_1 and E_2 branches respectively, and two B_1 branches. The B_1 modes are Infrared-Raman inactive singlets, therefore, it is silent whereas nonpolar E_2 branches are the only Raman active doublet modes with E_2 ; high and low. These correspond to oxygen atoms and zinc sub-lattices vibrations, respectively. The Infrared-Raman active A_1 and E_1 branches are polar. Therefore, long-range Coulomb electrostatic field lead to A_1 and E_1 splitting into longitudinal optical and transverse optical modes with different frequencies [2, 49–51].

Figure 5 shows the Raman spectra of ZnO samples. The 439 cm^{-1} most predominant peak, which is the signature of intrinsic property of wurtzite crystal structure, indicates the ZnO nonpolar optical phonon modes (high frequency E_2 mode) which is emanated from oxygen atoms movement. The peaks at $332, 333, 334$ and 338 cm^{-1} correspond to vibrations originated from the difference of two strongest modes; $E_2(\text{high}) - E_2(\text{low})$, a second order multiple phonon scattering process with some Raman shifts. The spectra at $330\text{--}340\text{ cm}^{-1}$ relates to second-order phonon of the E_2 low frequency. The peaks detected at 384 and 386 cm^{-1} correspond to the vibrational A_1 transverse optical mode. The first-order Raman modes band occurring

between 570 and 580 cm^{-1} (peaks seen at $570, 575, 577$ and 578 cm^{-1}) correspond to longitudinal optical modes of A_1 and E_1 symmetry caused by zinc interstitials or oxygen vacancies; defects and impurities. Yao-Ming Hao et al. [2] and Shuxia et al. [52] showed the peaks in between $500\text{--}600$ and 528 cm^{-1} were found to be originating from the vibrational modes of Mn^{2+} ions present in ZnO lattices which is not discovered in pristine ZnOs. But in contradiction to the above statement, a broad peak is seen in the range of $525\text{--}535\text{ cm}^{-1}$ only in pristine ZnO– NaBH_4 . This peak corresponds to the vibrational mode of $2 \times \text{LA}$ in bulk ZnO scattering. Therefore, this vibrational peak seen only in ZnO– NaBH_4 may be originated due to the native defects which may be generated due to the evolution of hydrogen gases during the reaction when NaBH_4 solution was added directly to zinc acetate solution but further study is needed for confirmation. A broad peak above 600 cm^{-1} in ZnO– NaBH_4 sample is found to be due to the acoustic overtone.

ESR spectroscopy, a technique used to study unpaired electrons presence in any material i.e. paramagnetic defects or characterizing magnetic properties developed from defect centers in atomic scale. Some of the defect centers include surface defects, impurity atoms or dopants, radicals; organic or inorganic, oxygen vacancies etc. Pure ZnO possesses non-magnetic behaviour; however, they respond to ESR spectroscopy by exhibiting distinguished ESR peaks due to the presence of defects (singly charge) which can be intrinsic or extrinsic in nature. The native defects present in pure ZnO structures are intrinsic defects which are zinc and oxygen vacancies/interstitials and some are extrinsic created by doping. The ESR spectra reveal linearly correlating information about the relationship between optical and electronic properties [1, 53] originating from defects present in crystal structure. From Fig. 6, the g -factor which is also known as Landè factor is calculated by using $g = (h\nu) / (\mu B)$ formula; where $h\nu$ = energy absorb by the electron, (h = Planck’s constant = $6.626 \times 10^{-34}\text{ J.s}$, ν = microwave frequency = 8.75 GHz for X-band measurement, μ = Bohr magneton constant = $9.2741 \times 10^{-24}\text{ JT}^{-1}$, B = magnetic field in mT). These broad ESR spectra shown in Fig. 5 results in almost same g value of $g_1 = 2.0359$ (ZnO– NaOH), $g_2 = 2.0267$ (ZnO– N_2H_4), $g_3 = 2.0212$ (ZnO– NaBH_4), and $g_4 = 1.972$ (ZnO– $\text{Li}(\text{C}_2\text{H}_5)_3\text{BH}$). These values of g_1, g_2 and g_3 are found to be close with free electrons g value ($g = 2.0023$) which contributes a little orbital magnetic moment. These g_1, g_2 and g_3 are found in between 2.007 and 2.05 that correspond to the chemisorbed oxygen molecules in ZnO surface. However, the spectra of ZnO– $\text{Li}(\text{C}_2\text{H}_5)_3\text{BH}$ resulting at $g_4 = 1.972$ (a very close value to $g = 1.6$) can be concluded that it is associated with the oxygen vacancies in ZnO structures. This concluded result

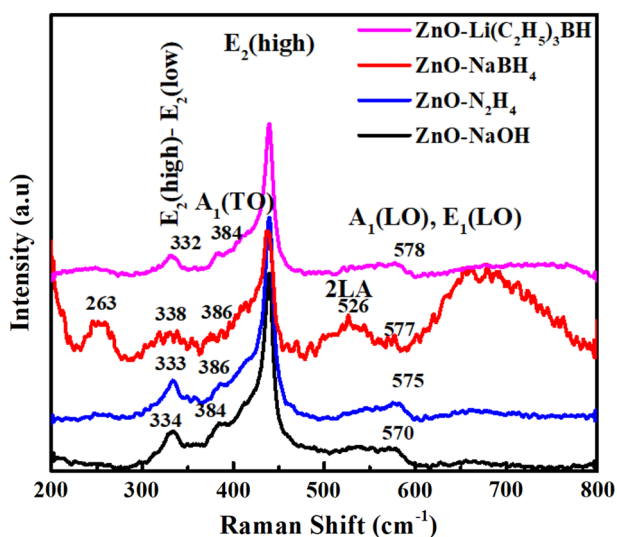


Fig. 5 Raman spectra of spindle shaped ZnO samples

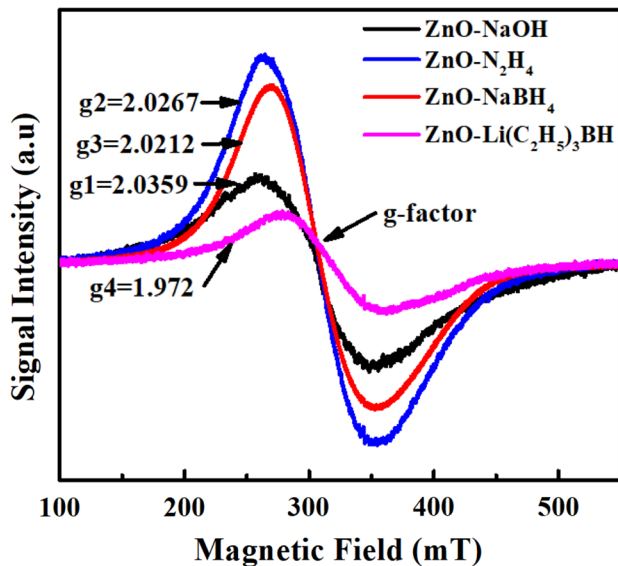


Fig. 6 ESR spectra of spindle shaped ZnO samples

is being supported by Raman spectra study (Fig. 5) and PL spectra studied in previously published article [15]. The photoluminescence spectra showed near band emission and a broad visible emission which was originated from defects. The defect emissions were affected by the use of different reducing agents and ZnO-N₂H₄ sample showed higher intensity of defect emission as compared to other samples [15]. Also from Fig. 6 it is clearly observed that the intensities of ESR spectra for all ZnO samples are varied. The intensity of g₄ is ~ 1/4 of g₂, ~ 1/3 of g₃ and ~ 1/2 of g₁. Among all the oxygen defects, singly charge oxygen defect or vacancy shows paramagnetic behaviour and therefore it can be easily detected by ESR spectroscopy [54–56].

From all the above analysis and discussion, a simple nanoparticle formation can be concluded based on the nucleation and growth rate. Here, it can be summarized that the pH of the synthesis medium and reaction time play significant roles in producing a proper structure with uniform size distributions. The zinc source, Zn(CH₃COO)₂ are being dissociated into zinc and acetate ions when dissolve in the ethylene glycol solvent at 60–70 °C. The solvent ethylene glycol acts as a surfactant by attaching the glycol functional groups to the zinc hydroxide surfaces throughout the nucleation and growth process inhibiting from aggregation and controlling steady growth. The nucleation process takes place when the reducing agent solution is slowly added to the zinc acetate solution where hydrolysis of base takes place. However, as the rate of nucleation depends upon the reducing ability of the newly introduced base solution, the nucleation rate when NaOH is used is lower than Li(C₂H₅)₃BH which is

known as a strong base and better reducing ability. The crystal growth rate of Zn(OH)₂ nuclei to a uniform particle formation is slowed in the case of NaOH but it is found to be fully grown into a perfect fusiform structure in the presence of strong bases NaBH₄ or N₂H₄ or Li(C₂H₅)₃BH. The formation of Zn(OH)₂ nuclei which precipitated into fully grown structures can occur in various processes like anion exchange and anion substitution [57]. The minor difference in size distribution can also be the result of the difference in the reducing ability of the three reducing agents by a factor of intermediate complex formation rate which needs to be studied systematically. This concept can also be explained by a slow or rapid process of hydrolysis of the base or reducing agents. The formation of a particular shape of ZnO may be due to the action of solvent (ethylene glycol) as the use of water in ZnO formation can lead to the formation of rods or tube shape structure (elongated in a particular direction) and the use of diethylene glycol can form nanosphere structures as reported in the previous article [15]. The reaction time taken i.e. 2 h is found to be sufficient enough to form stable Zn(OH)₂ fusiform structure which give ZnO when dehydrated by the strong reducing agents. However, the complete formation of uniform fusiform structure cannot be seen in the case of NaOH yet forming stable incomplete fusiform ZnO structure [3, 15, 31, 57].

The synthesised ZnOs were annealed at 300 °C for 6 h before using as a catalyst in photo-catalytic degradation of rhodamine B (RhB) and methylene blue (MB) dyes. ZnOs were annealed to remove moisture content in these samples and to burn the remaining glycol coatings on nanoparticle surfaces. The annealing process can enhance photo-catalytic activity of ZnOs under UV light following a batch system reaction. Figure 7 illustrates complete setup for dye degradation in a batch reactor system where UV lamp is placed directly above dye solution. The colloidal solution is stirred continuously to prevent aggregation/sedimentation of the catalyst and assist in uniform distribution of catalyst. The degradation rate of 10 ppm MB and RhB dye solution in presence of 50 mg annealed ZnO (A-ZnO) particles is illustrated in Fig. 8(a) methylene blue and (b) rhodamine B. The rate of complete decolourisation and degradation differs with different modelled dyes used due to their different compositions and interaction with the catalyst molecules. MB and RhB dyes took 100–140 min and 150–170 min respectively. The chemical formulae of MB (molar mass = 319.85 g) and RhB (molar mass = 479.02 g) are C₁₆H₁₈ClN₃S and C₂₈H₃₁ClN₂O₃ respectively with different chemical structures. The difference in degradation time is due to different compositions and chemical structures of both organic dyes. The degradation rate is also highly depended on the amount of dye molecules absorbed

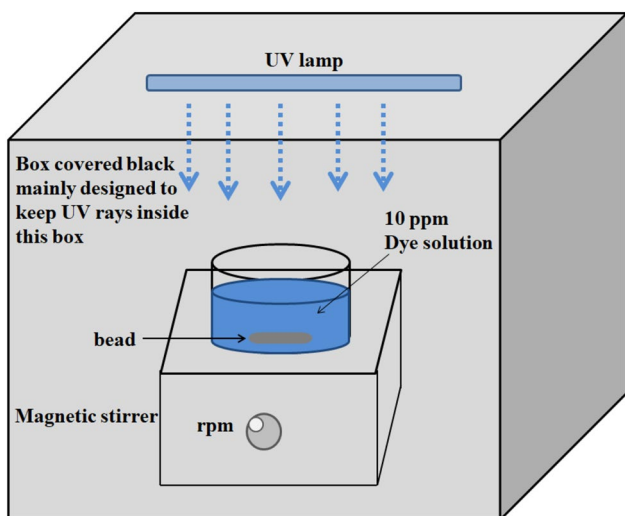


Fig. 7 Illustration of dye degradation setup with UV lamp

by the catalyst either in surface or in holes or defects. As MB has a smaller molecular structure as compared to bulky RhB structure, more number of dye molecules gets penetrated inside the catalyst and onto the surface [58]. Therefore, the number of dye molecules absorbing or in contact with ZnO surface and pores is more for MB and less for RhB, illustrated by Fig. 9(a) Methylene blue, and (b) Rhodamine B. The RhB degradation takes place in two reaction steps: (1) gradual diethylation and (2) chromophore structure decomposition when the reactive oxygen species (ROS) generated in the reaction medium during the light illumination. But MB degradation goes through only step (2) chromophore structure decomposition [59] where chromophore decomposition consists of double bond breaking present in benzene ring.

Therefore, degradation of RhB takes more time as compared to degradation of MB. Figure 10a shows the molecular degradation of RhB, and the possible intermediates formed when chromophore cleavage process takes place are given by the molecular structures. The mineralization would dominate the reaction steps by opening the benzene rings when react with reactive oxygen species. The ROS species are peroxides; containing O–O group (ex. H₂O₂), superoxides; O²⁻ which can be resulted by converting molecular oxygen to superoxide anion radical, hydroxyl anion/hydroxyl radical; OH⁻/OH[·] generated by hydrogen peroxide with an acceptance of electron. The molecular degradation of MB and its intermediate products are shown in Fig. 10b. The chromophore cleavage formation is followed by ring opening and resulted in the mineralization into less harmful products like CO, CO₂ and H₂O. The Eqs. 8, 9 and 10 show the process of generating electron and hole pairs when adequate amount of energy is supplied by the light source and inducing in generating insitu reactive oxygen species, and thereby resulting in bond breaking of dye molecules mineralizing them into less harmful by-products [60].

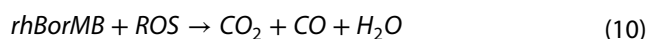
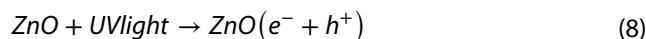


Table 2 gives the comparison of the time taken for complete decolourisation of methylene blue dye by ZnO photocatalysts under UV light before and after annealing the ZnO sample. The comparison of degradation rate constants for MB dye degradation is given in Table S1

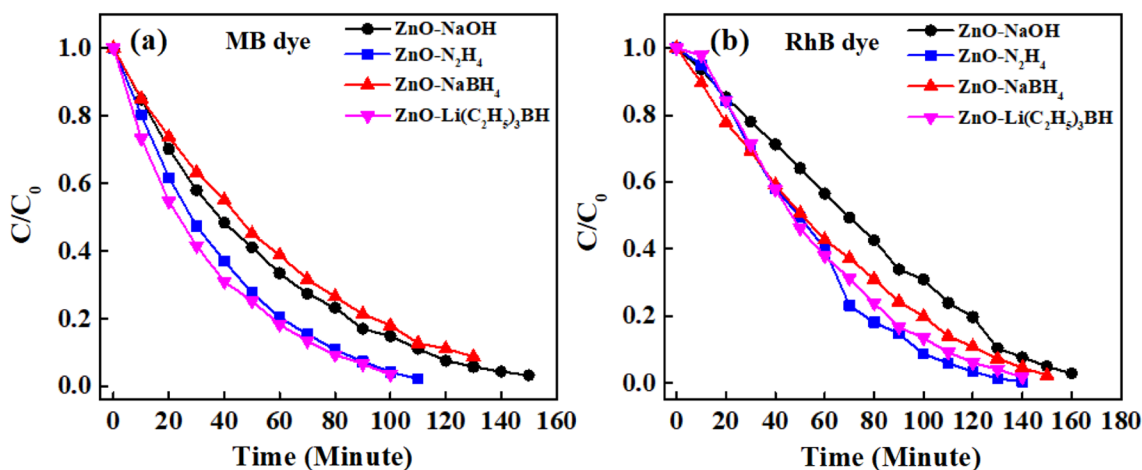


Fig. 8 Photo-catalytic degradation of a Methylene blue MB, b Rhodamine B RhB under UV light illumination in the presence of annealed ZnO catalyst (A-ZnO)

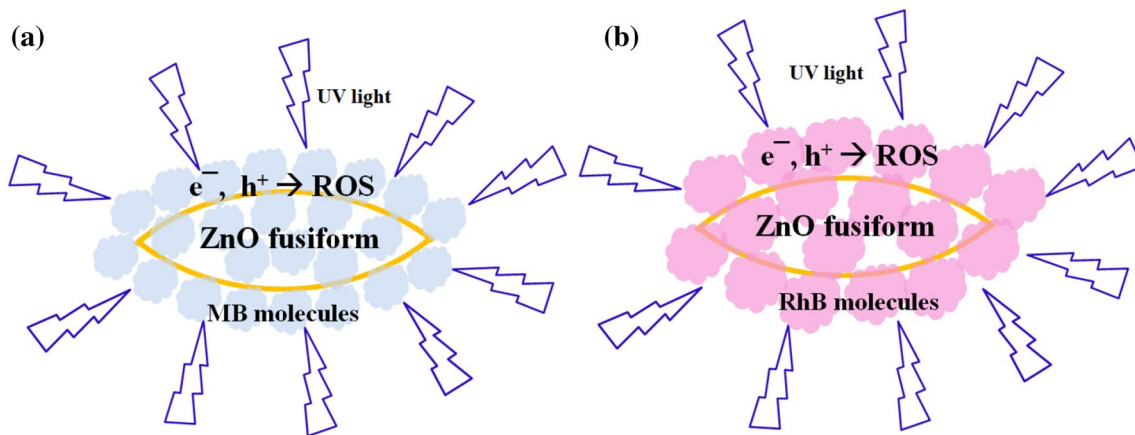


Fig. 9 Schematic diagram of **a** Methylene blue MB, **b** Rhodamine B (RhB) dye molecules attaching to ZnO fusiform structure with UV light illumination

(supplementary information) calculated from the pseudo first order chemical kinetics reaction equation;

$$\ln(C_0/C) = kt \quad (11)$$

where k = degradation rate constant in min^{-1} , C_0 = initial concentration and C = concentration at time t . It is evident from Table 2, Table S1 and Fig. S1 that un-annealed ZnO photocatalyst take more time to degrade dye solution as compared to the annealed ZnO photocatalyst under the same experimental conditions. Various factors such as surface area, porosity, particle size, morphologies, defects etc. can influence the rate of degradation for complete degradation of hazardous dye molecules present in water [3, 14–16, 21, 31, 32]. However, the scope of improving above said process is limitless. It is also important to pinpoint the exact factor that can cause effective degradation, but it can be concluded that photocatalytic degradation process is a collective effort for all factors to give a complete degradation in less amount of time efficiently and more effectively. Due to the dependence of degradation rate to the rate of photo-generated electrons and holes recombination after the generation of electrons and holes when light of sufficient energy is illuminated into the photocatalysts material, the existence of crystal/native defects in ZnO can enhance degradation mechanism by inhibiting recombination process. Therefore, generation of reactive oxygen species (ROS) which are chemically active oxygen containing chemical species are a major breakthrough in photo-catalysis process which majorly depends upon the production capability of peroxides during the reaction in the solution. It is also well known that annealing process enhances the crystal quality accompanied with a change in surface defects [31, 32, 61] and it has also been proved by our earlier research work and this article that annealed ZnO takes 100–140 min and simple ZnO takes around

160–180 min to degrade the same 50 ml of 10 ppm MB dye solution under the same UV light frequency and intensity [15]. The comparison of the time taken is given by Table 2 and degradation of MB using un-annealed ZnO is shown in Fig. S1 (supplementary information). As the quantitative analysis of defects in ZnO samples is quite complicated and partially explained through PL spectra, Raman and ESR spectroscopy, this application is carried out in continuation with the previous research to show the dependence of photocatalytic semiconductor properties on photocatalysis, and effect of dye molecular structure on degradation rate. The annealed ZnO nanomaterials possess better and efficient photo-catalytic degradation toward MB and RhB as compared to un-annealed ZnO nanomaterials.

4 Conclusion

The morphological and physico-chemical properties of zinc oxides are found to vary with different reducing agents used in the facile chemical synthesis process. Hydroxyl group (–OH) functionalized spindle shaped ZnO with various dimensions are formed employing reducing agents viz. sodium hydroxide, hydrazine hydride, sodium borohydride and lithium triethyl borohydride resulting in various basicity level in ethylene glycol solvent during the reaction. Irregular ZnO structure is observed in presence of NaOH unlike other reducing agents that produces perfect spindle shape ZnO morphologies as shown in SEM and TEM images. This can be due to the low reducing ability of NaOH as compared to other reducing agents producing stable fully formed fusiform structures. By studying ESR peaks and Raman vibrational modes, it is evident that pristine ZnO samples show the presence of crystal imperfections like defects which are either native (intrinsic) defects

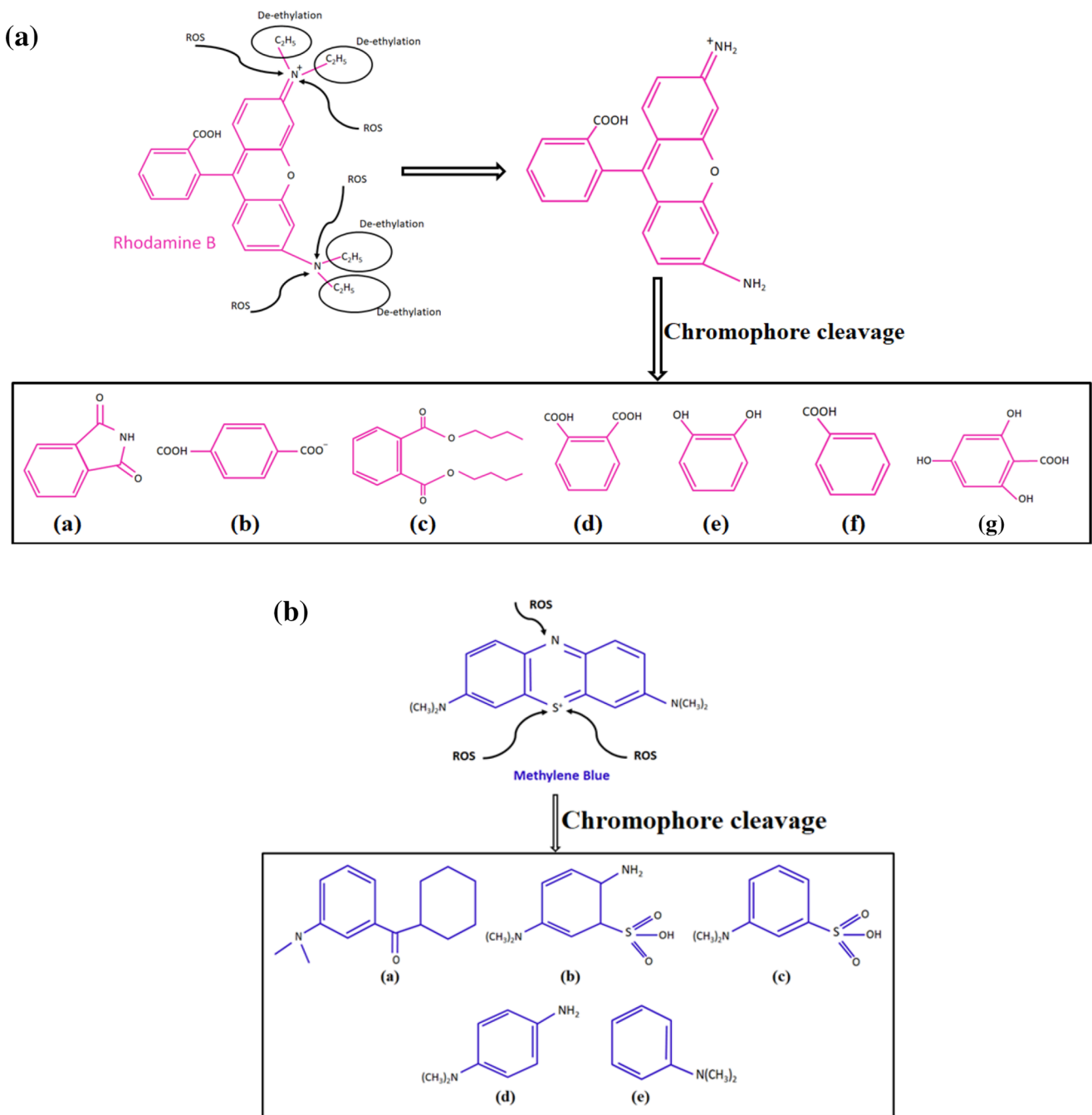


Fig. 10 **a** Rhodamine B degradation and **b** Methylene blue dye degradation

Table 2 Time taken for complete decolourisation of methylene blue dye when treated with different photocatalyst ZnO sample

Sl. No.	Sample name	Complete decolourisation (min)	
		Before calcination	After calcination
1.	ZnO–NaOH	170–180	150–160
2.	ZnO–N ₂ H ₄	150–160	100–110
3.	ZnO–NaBH ₄	140–160	130–140
4.	ZnO–Li(C ₂ H ₅) ₃ BH	120–130	100–110

or chemisorbed oxygen molecules. Further study shows that annealing process helps in speeding photo-catalytic degradation of MB and RhB dyes under UV illumination which is concluded after comparing with previous work of photo-catalytic degradation of MB dye before ZnOs were annealed. The photo-catalytic degradation of RhB dye takes more time than MB even in the presence of photo-catalyst. From the study, it is being concluded that due to different chemical molecular structures and compositions

of RhB and MB, RhB dye molecules were able to absorb in less numbers in the catalyst surfaces thereby consuming more time in degradation and also annealing process can speed up the degradation reaction.

Acknowledgements The authors acknowledge and thank the help and facility given by the Sophisticated Analysis Instruments Facility, IIT Bombay, for providing such analytical facilities.

Compliance with ethical standards

Conflict of interest There is no conflict of interest between the authors.

References

- Ischenko V, Polarz S, Grote D, Stavarache V, Fink K, Driess M (2005) Zinc oxide nanoparticles with defects. *Adv Func Mater* 15:1945–1954
- Hao YM, Lou SY, Zhou SM, Yuan RJ, Zhu GY, Li N (2012) Structural, optical, and magnetic studies of manganese-doped zinc oxide hierarchical microspheres by self-assembly of nanoparticles. *Nanoscale Res Lett* 7:1–9
- Rani B, Punniyakoti S, Sahu NK (2018) Polyol asserted hydrothermal synthesis of SnO₂ nanoparticles for the fast adsorption and photocatalytic degradation of methylene blue cationic dye. *New J Chem* 42:943–954
- Muniz EC, Góes MS, Silva JJ et al (2011) Synthesis and characterization of mesoporous TiO₂ nanostructured films prepared by a modified sol–gel method for application in dye solar cells. *Ceram Int* 37:1017–1024
- Manoharan G, Karupiah M, Sahu NK, Hembram K (2018) High performance multi-layer varistor (MLV) from doped ZnO nanopowders by water based tape casting: rheology, sintering, microstructure and properties. *Ceram Int* 44:7837–7843
- Sahu K, Singh J, Mohapatra S (2019) Photocatalytic and catalytic removal of toxic pollutants from water using CuO nanosheets. *J Mater Sci: Mater Electron* 30:6088–6099
- Szilágyi IM, Fórizs B, Rosseler O et al (2012) WO₃ photocatalysts: influence of structure and composition. *J Catal* 294:119–127
- Beek W, Wienk M, Janssen RAJ (2004) Efficient hybrid solar cells from zinc oxide nanoparticles and a conjugated polymer. *Adv Mater* 16(12):1009–1013
- Aparna ML, Grace AN, Sathyanarayanan P, Sahu NK (2018) A comparative study on the supercapacitive behaviour of solvothermally prepared metal ferrite (MFe₂O₄, M = Fe, Co, Ni, Mn, Cu, Zn) nanoassemblies. *J Alloy Compd* 745:385–395
- Jiang X, Wong F, Fung M, Lee S (2003) Aluminum-doped zinc oxide films as transparent conductive electrode for organic light-emitting devices. *Appl Phys Lett* 83:1875–1877
- Wei A, Pan L, Huang W (2011) Recent progress in the ZnO nanostructure-based sensors. *Mater Sci Eng, B* 176:1409–1421
- Lupan O, Emelchenko G, Ursaki V et al (2010) Synthesis and characterization of ZnO nanowires for nanosensor applications. *Mater Res Bull* 45:1026–1032
- Gupta J, Bhargava P, Bahadur D (2015) Fluorescent ZnO for imaging and induction of DNA fragmentation and ROS-mediated apoptosis in cancer cells. *J Mater Chem B* 3:1968–1978
- Becheri A, Dürr M, Nostro PL, Baglioni P (2008) Synthesis and characterization of zinc oxide nanoparticles: application to textiles as UV-absorbers. *J Nanopart Res* 10:679–689
- Thongam DD, Gupta J, Sahu NK, Bahadur D (2018) Investigating the role of different reducing agents, molar ratios, and synthesis medium over the formation of ZnO nanostructures and their photo-catalytic activity. *J Mater Sci* 53:1110–1122
- Gupta J, Bahadur D (2017) Visible light sensitive mesoporous Cu-substituted ZnO nanoassembly for enhanced photocatalysis, bacterial inhibition, and noninvasive tumor regression. *ACS Sustain Chem Eng* 5:8702–8709
- Kuriakose S, Sahu K, Khan SA, Tripathi A, Avasthi DK, Mohapatra S (2017) Facile synthesis of Au–ZnO plasmonic nanohybrids for highly efficient photocatalytic degradation of methylene blue. *Opt Mater* 64:47–52
- Kuriakose S, Choudhary V, Satpati B, Mohapatra S (2014) Enhanced photocatalytic activity of Ag–ZnO hybrid plasmonic nanostructures prepared by a facile wet chemical method. *Beilstein J Nanotechnol* 5:639–650
- Singh N, Pai MR, Kaur G et al (2019) Z_{n1-x}Fe_xO_y nanocomposites for renewable hydrogen produced efficiently via photoelectrochemical vis-a-vis photocatalytic splitting of water. *SN Appl Sci* 1:611
- Kuriakose S, Satpati B, Mohapatra S (2014) Enhanced photocatalytic activity of Co doped ZnO nanodisks and nanorods prepared by a facile wet chemical method. *Phys Chem Chem Phys* 16:12741–12749
- Kuriakose S, Satpati B, Mohapatra S (2015) Highly efficient photocatalytic degradation of organic dyes by Cu doped ZnO nanostructures. *Phys Chem Chem Phys* 17:25172–25181
- Liu H, Fan H, Wu R, Tian L, Yang X, Sun Y (2019) Nitrogen-doped black TiO₂ spheres with enhanced visible light photocatalytic performance. *SN Appl Sci* 1:487
- Xi G, Yue B, Cao J, Ye J (2011) Fe₃O₄/WO₃ hierarchical core-shell structure: high-performance and recyclable visible-light photocatalysis. *Chem A Eur J* 17(18):5145–5154
- Pan C, Xu J, Wang Y, Li D, Zhu Y (2012) Dramatic activity of C₃N₄/BiPO₄ photocatalyst with core/shell structure formed by self-assembly. *Adv Funct Mater* 22(7):1518–1524
- Srikant V, Clarke DR (1998) On the optical band gap of zinc oxide. *J Appl Phys* 83:5447–5451
- Ismail A, Abdullah M (2013) The structural and optical properties of ZnO thin films prepared at different RF sputtering power. *J King Saud Univ Sci* 25:209–215
- Raoufi D (2013) Synthesis and microstructural properties of ZnO nanoparticles prepared by precipitation method. *Renew Energy* 50:932–937
- Zhang L, Yin L, Wang C, Lun N, Qi Y, Xiang D (2010) Origin of visible photoluminescence of ZnO quantum dots: defect-dependent and size-dependent. *J Phys Chem C* 114:9651–9658
- Erhart P, Klein A, Albe K (2005) First-principles study of the structure and stability of oxygen defects in zinc oxide. *Phys Rev B* 72:085213
- Lin B, Fu Z, Jia Y (2001) Green luminescent center in undoped zinc oxide films deposited on silicon substrates. *Appl Phys Lett* 79:943–945
- Gupta J, Barick KC, Bahadur D (2011) Defect mediated photocatalytic activity in shape-controlled ZnO nanostructures. *J Alloy Compd* 509:6725–6730
- Rahman QI, Ahmad M, Misra SK, Lohani M (2013) Effective photocatalytic degradation of rhodamine B dye by ZnO nanoparticles. *Mater Lett* 91:170–174
- Wang Y, Hou C, Lin X, Jiang H (2019) Photocatalytic decomposition of rhodamine B by newly designed one-dimension ZnO using chemical method. *SN Appl Sci* 1:743
- Vadivel S, Vanitha M, Muthukrishnaraj A, Balasubramanian N (2014) Graphene oxide–BiOBr composite material as highly efficient photocatalyst for degradation of methylene blue and rhodamine-B dyes. *J Water Process Eng* 1:17–26

35. Rani S, Aggarwal M, Kumar M, Sharma S, Kumar D (2016) Removal of methylene blue and rhodamine B from water by zirconium oxide/graphene. *Water Sci* 30:51–60
36. Gupta VK, Suhas I Ali, Saini VK (2004) Removal of Rhodamine B, fast green, and methylene blue from wastewater using red mud, an aluminum industry waste. *Ind Eng Chem Res* 43:1740–1747
37. Suresh P, Sujana Kumari U, Siva Rao T, Prasada Rao AV (2015) Rapid sun light degradation of Rhodamine-B, methylene blue, methyl orange, congo red and their binary mixtures using suprathermochemical Bi-Molybdate. *Int J Eng Appl Sci* 2:42–46
38. Bindu P, Thomas S (2014) Estimation of lattice strain in ZnO nanoparticles: X-ray peak profile analysis. *J Theor Appl Phys* 8:123–134
39. Sahai A, Goswami N (2014) Structural and vibrational properties of ZnO nanoparticles synthesized by the chemical precipitation method. *Physica E* 58:130–137
40. Rajeswari Yogamalar N, Chandra Bose A (2011) Tuning the aspect ratio of hydrothermally grown ZnO by choice of precursor. *J Solid State Chem* 184:12–20
41. Yogamalar R, Srinivasan R, Vinu A, Ariga K, Bose AC (2009) X-ray peak broadening analysis in ZnO nanoparticles. *Solid State Commun* 149:1919–1923
42. John R, Rajakumari R (2012) Synthesis and characterization of rare earth ion doped nano ZnO. *Nano-Micro Lett* 4:65–72
43. Gnanasangeetha D, SaralaThambavani D (2013) One pot synthesis of zinc oxide nanoparticles via chemical and green method. *Res J Mater Sci* 2320:6055
44. Babu KS, Narayanan V (2013) Hydrothermal synthesis of hydrated zinc oxide nanoparticles and its characterization. *Chem Sci Trans* 2:533–536
45. Xiong G, Pal U, Serrano J, Ucer K, Williams R (2006) Photoluminescence and FTIR study of ZnO nanoparticles: the impurity and defect perspective. *Physica Status Solidi (c)* 3:3577–3581
46. Ivanova T, Harizanova A, Koutzarova T, Vertruyen B (2010) Study of ZnO sol–gel films: effect of annealing. *Mater Lett* 64:1147–1149
47. Carroll KJ, Reveles JU, Shultz MD, Khanna SN, Carpenter EE (2011) Preparation of elemental Cu and Ni nanoparticles by the polyol method: an experimental and theoretical approach. *J Phys Chem C* 115:2656–2664
48. Bundesmann C, Ashkenov N, Schubert M et al (2003) Raman scattering in ZnO thin films doped with Fe, Sb, Al, Ga, and Li. *Appl Phys Lett* 83(10):1974–1976
49. Decremps F, Pellicer-Porres J, Saitta AM, Chervin J-C, Polian A (2002) High-pressure Raman spectroscopy study of wurtzite ZnO. *Phys Rev B* 65:092101
50. Rajalakshmi M, Arora AK, Bendre B, Mahamuni S (2000) Optical phonon confinement in zinc oxide nanoparticles. *J Appl Phys* 87:2445–2448
51. Das S, Das S, Sutradhar S (2017) Enhanced dielectric behavior and ac electrical response in Gd–Mn–ZnO nanoparticles. *J Alloy Compd* 726:11–21
52. Guo S, Du Z, Dai S (2009) Analysis of Raman modes in Mn-doped ZnO nanocrystals. *Physica Status Solidi (b)* 246(10):2329–2332
53. Zheng M, Zhang L, Li G, Shen W (2002) Fabrication and optical properties of large-scale uniform zinc oxide nanowire arrays by one-step electrochemical deposition technique. *Chem Phys Lett* 363:123–128
54. Repp S, Erdem E (2016) Controlling the exciton energy of zinc oxide (ZnO) quantum dots by changing the confinement conditions. *Spectrochim Acta Part A Mol Biomol Spectrosc* 152:637–644
55. Djurišić AB, Choy WC, Roy VAL et al (2004) Photoluminescence and electron paramagnetic resonance of ZnO tetrapod structures. *Adv Func Mater* 14:856–864
56. Drouilly C, Krafft J-M, Averseng FD et al (2012) ZnO oxygen vacancies formation and filling followed by in situ photoluminescence and in situ EPR. *J Phys Chem C* 116:21297–21307
57. Liang M-K, Limo MJ, Sola-Rabada A, Roe MJ, Perry CC (2014) New insights into the mechanism of ZnO formation from aqueous solutions of zinc acetate and zinc nitrate. *Chem Mater* 26:4119–4129
58. Wang S, Boyjoo Y, Choueib A (2005) A comparative study of dye removal using fly ash treated by different methods. *Chemosphere* 60:1401–1407
59. Ganesh RS, Durgadevi E, Navaneethan M et al (2017) Visible light induced photocatalytic degradation of methylene blue and rhodamine B from the catalyst of CdS nanowire. *Chem Phys Lett* 684:126–134
60. Carneiro JO, Samantilleke AP, Parpot P et al (2016) Visible light induced enhanced photocatalytic degradation of industrial effluents (Rhodamine B) in aqueous media using TiO₂ nanoparticles. *J Nanomater* 2016:13
61. Yang J, Liu X, Yang L et al (2009) Effect of annealing temperature on the structure and optical properties of ZnO nanoparticles. *J Alloy Compd* 477:632–635

Publisher's Note Springer Nature remains neutral with regard to jurisdictional claims in published maps and institutional affiliations.